Figures and figure supplements

Characterisation of molecular motions in cryo-EM single-particle data by multi-body refinement in RELION

Takanori Nakane *et al*

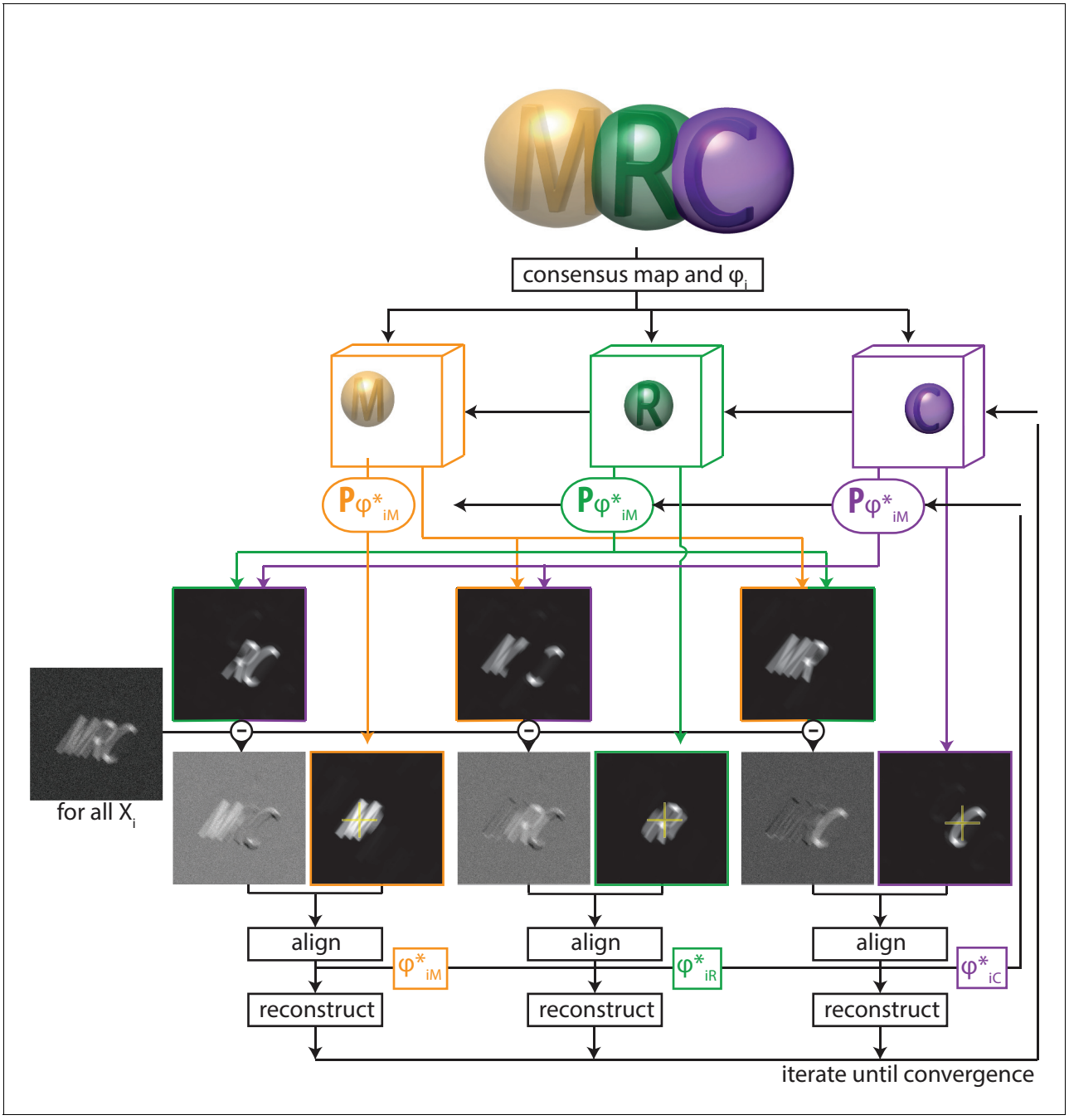

Figure 1. A schematic overview of multi-body refinement. After a consensus 3D auto-refinement in RELION, the three-dimensional consensus map is split into B separate bodies using user-defined masks. In this example, $B = 3$ and the letters 'M' (orange), 'R' (green) and 'C' (puple) each represent a body, and the corresponding spherical masks are shown with transparency. During multi-body refinement, one performs focused refinement for all experimental particle images X_i, with local rotational and translational searches around the orientations from the consensus refinement. The yellow crosses in the reference projections for the focused refinements of each body indicate the centre-of-mass of each body's mask, around which all rotations are made.For each body, partial signal subtraction is performed with projections along the current estimates for the respective orientations of the other $B - 1$ bodies. This leads to B subtracted versions of each experimental particle image during every iteration, which are aligned against projections of the corresponding body. The resulting optimal orientations ϕ_i^* for each body are used for the partial signal subtraction in the next iteration. Iterative alignment and reconstruction of all three bodiesis is repeated until convergence, which is when resolutions no longer improve and changes in the relative orientations of all bodies become small.

DOI: https://doi.org/10.7554/eLife.36861.002

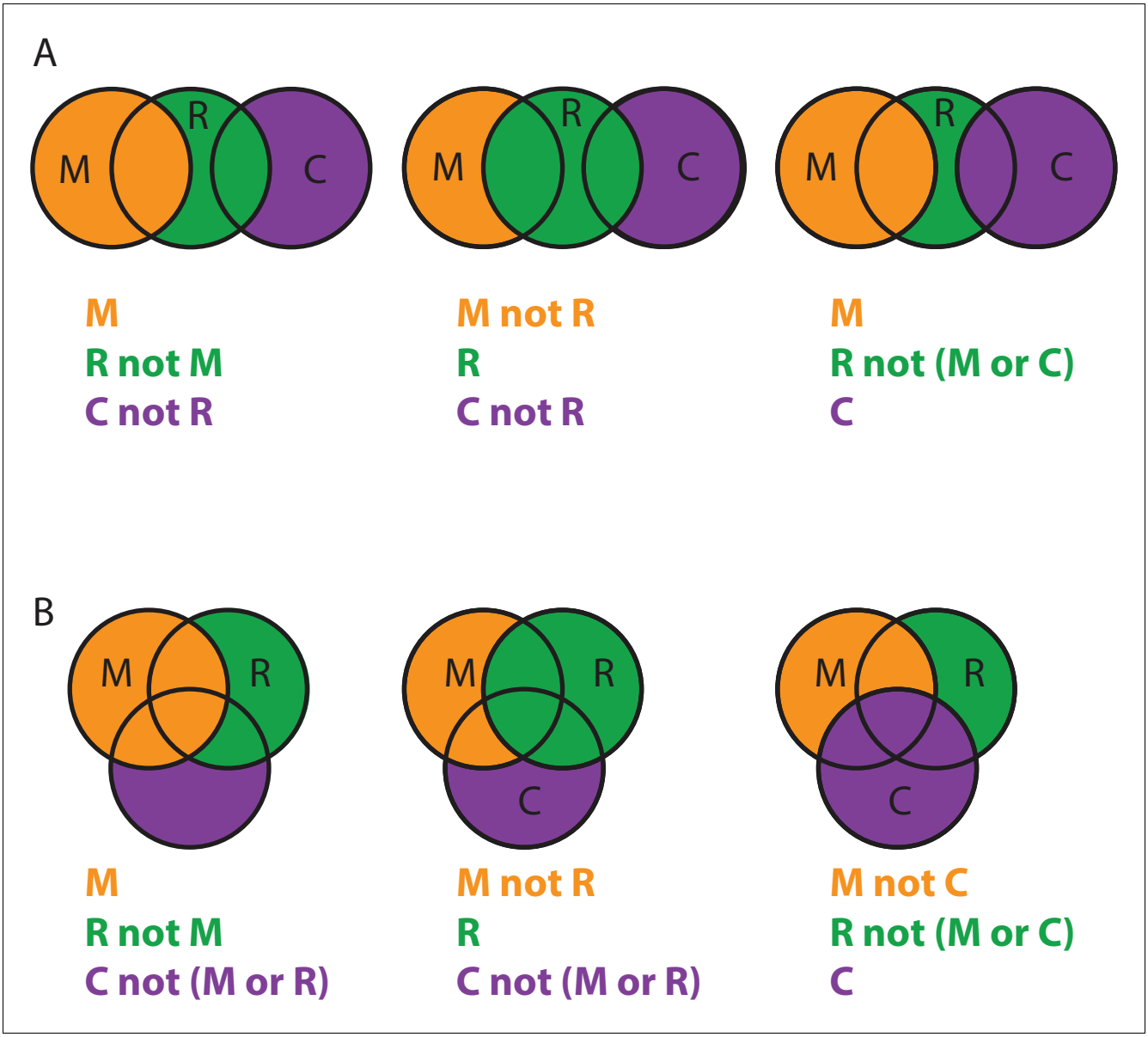

Figure 1—figure supplement 1. Overlapping body masks. (**A**) Overlapping masks for the example shown in ***Figure 1***. For the partial signal subtraction for focused refinement of the 'M' body, the density of the 'R' body within the 'R' mask but not within the 'M' mask will be subtracted, together with the density of the 'C' body within the 'C' mask, but not within the 'R' mask (left). Partial signal subtraction for focused refinement of the 'R' body comprises the density of the 'M' body within the 'M'mask that does not overlap with the 'R' mask and the density of the 'C' body within the 'C' mask that does not overlap with the 'R' mask (middle). Similarly, for focused refinement of the 'C' body, partial signal subtraction comprises the density of the entire 'M' body and the density of the 'R' body within the 'R' mask that does not overlap with either the 'M' mask or the 'C' mask. A total of seven different masked maps needs to be stored in computer memory. (**B**) As in A, but for an example whereall three masks overlap with each other. A total of nine different masked maps needs to be stored in computer memory.

DOI: https://doi.org/10.7554/eLife.36861.003

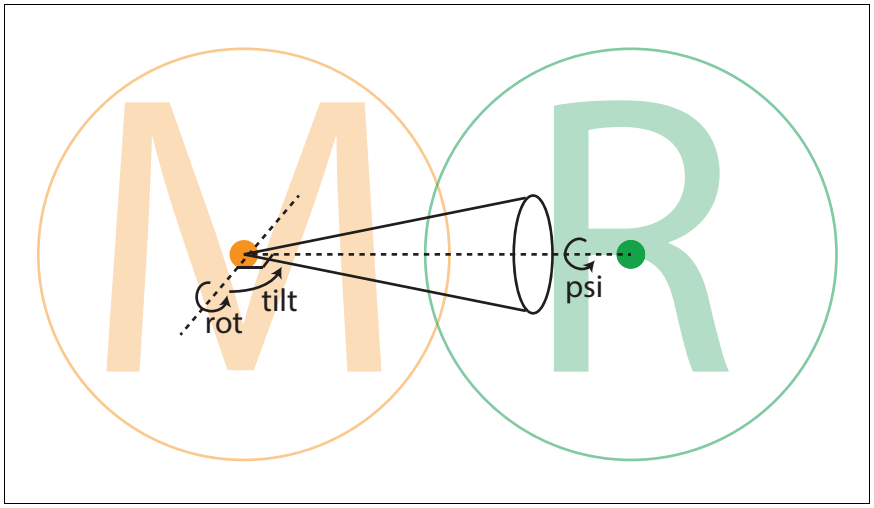

Figure 1—figure supplement 2. Relative body orientations. The density for each body is placed with the centre-of-mass of its mask (indicated with orange and green dots for the 'M' body and 'R' body, respectively) at the centre of the three-dimensional box, and all rotations are around this centre. Each body rotates relative to a neighbouring body, as defined using the rlnBodyRotateRelativeTo column in the input body STAR file (***Figure 1—source data 1***). In this example, the 'M' body rotates relative to the 'R' body. The rotation is expressed in Euler angles around an axis perpendicular to the vector between the centre-of-mass of the two bodies to prevent ambiguities in Euler-angle definitions around zero values for the second Euler angle (tilt). The cone illustrates the width at half the maximum value (FWHM) of a Gaussian-shaped prior on the rot-tilt tuple. A separate Gaussian-shaped prior exists on the third Euler angle (psi).

DOI: https://doi.org/10.7554/eLife.36861.004

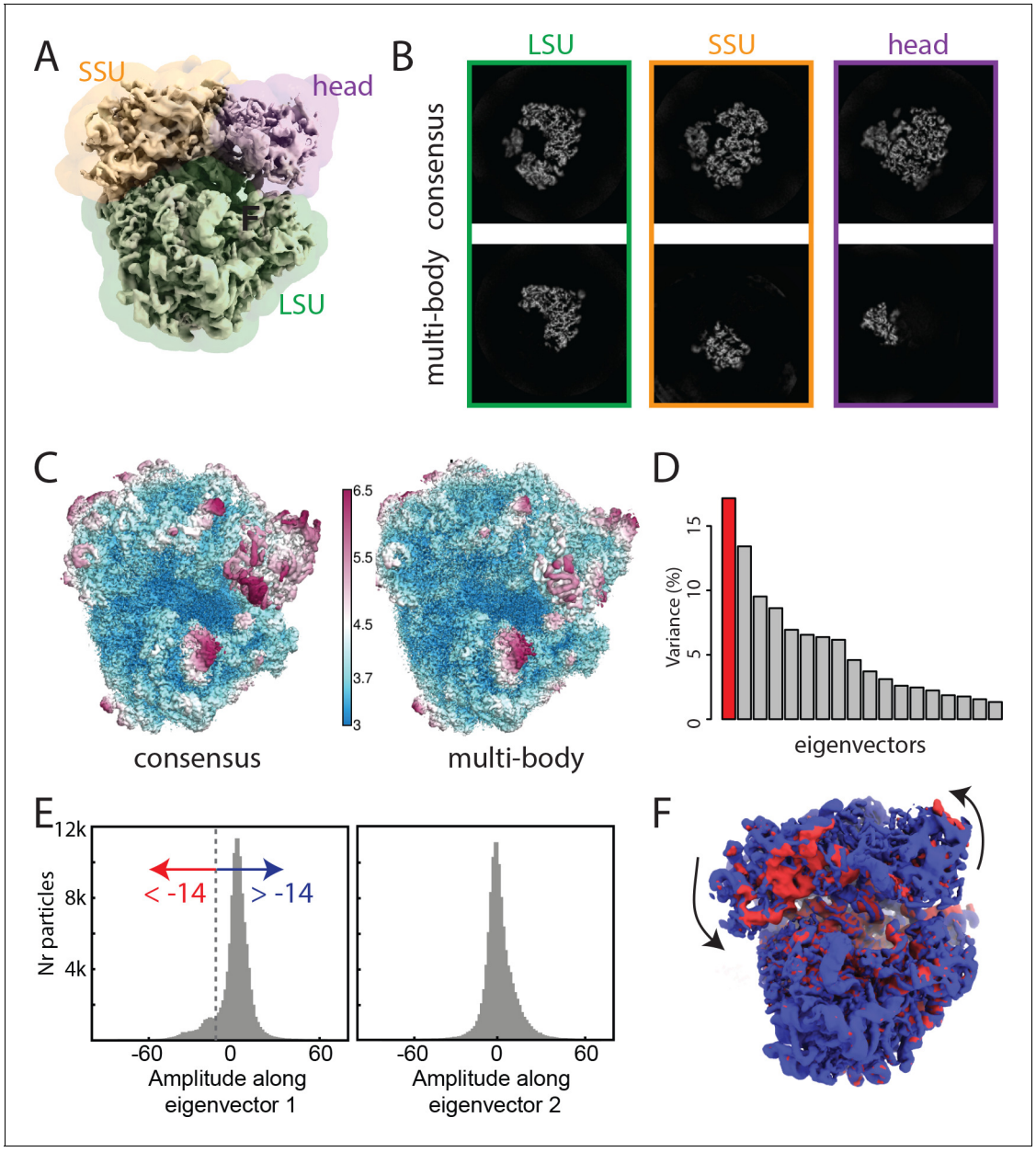

Figure 2. The ribosome test case. (**A**) The ribosome consensus map with the three transparent body masks (LSU, SSU and head) superimposed. (**B**) Slices through the density of the three bodies after the consensus refinement (top) and after multi-body refinement (down). (**C**) Local resolution estimates (in Å) calculated in RELION after the consensus refinement (left) and after multi-body refinement (right). (**D**) The contributions of all eigenvectors to the variance. The first eigenvector, for which the maps at the extremes are shown in panel F, is highlighted in red. (**E**) Histograms of the amplitudes along the first and second eigenvectors for all particle images in the data set. The histogram of the amplitudes along the first eigenvector shows a bimodal distribution. The data set was split into two subsets: particle images with the amplitude along the first eigenvector smaller than −14 (red arrow) and particle images with that amplitude larger than −14 (blue arrow). (**F**) Refined maps for the two subsets in the same colors. As observed in the movie along the first eigenvector, the SSU rolls with respect to the the LSU and the head swivels with respect to the SSU, *cf* ***Video 1***.

DOI: https://doi.org/10.7554/eLife.36861.006

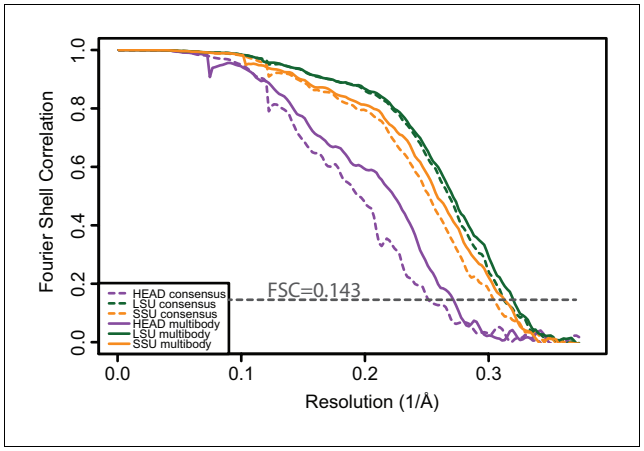

Figure 2—figure supplement 1. Fourier shell correlation curves calculated from independently refined halves of the data for the three bodies after consensus refinement (dashed lines) and after the second multi-body refinement (solid lines).

DOI: https://doi.org/10.7554/eLife.36861.007

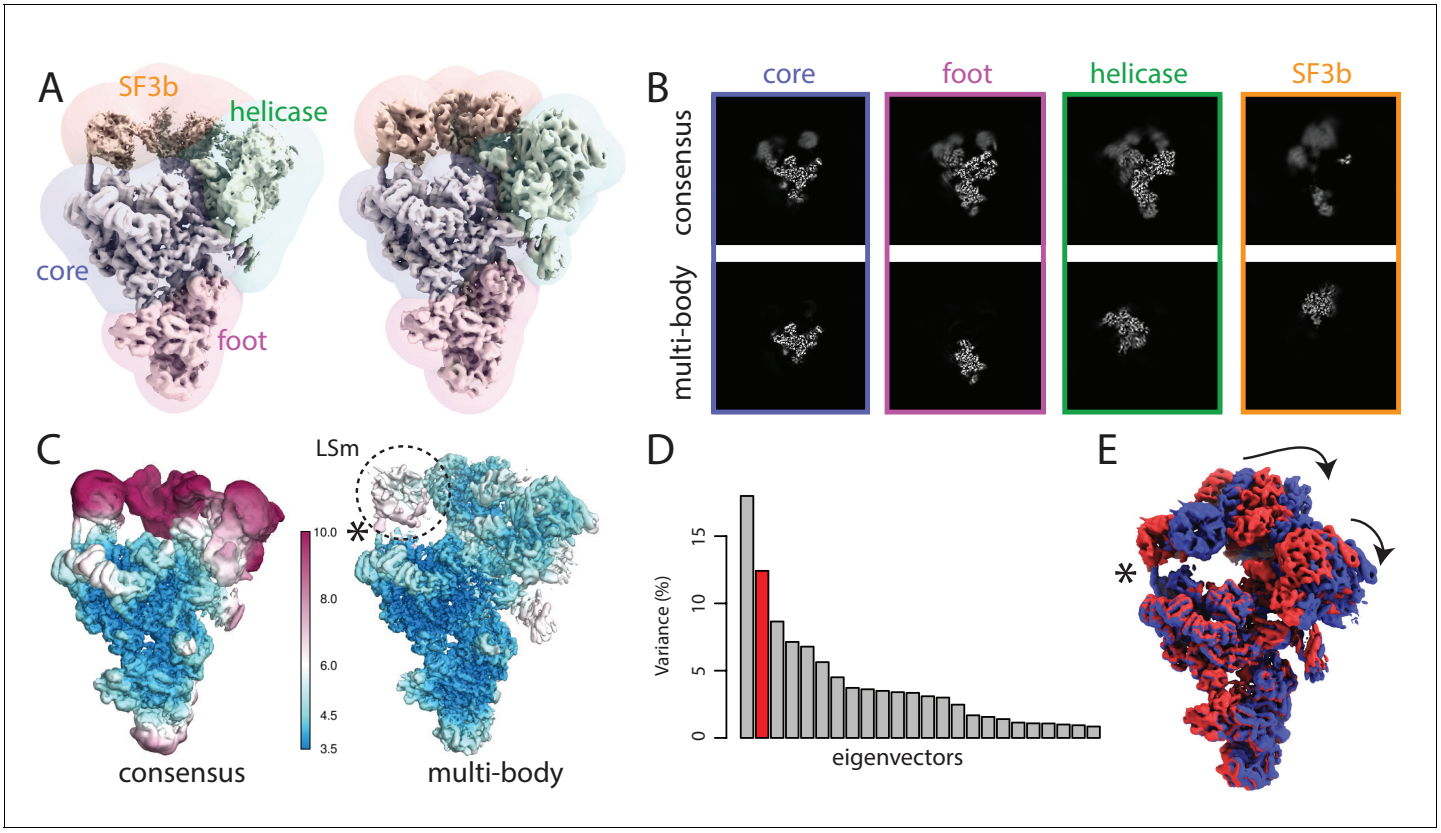

Figure 3. The spliceosome test case. (**A**) The four body masks used for the first splicesome multi-body refinement are shown in semi-transparent colours on top of the consensus map on the left; the resulting density after the first multi-body refinement and the masks used for the second multi-body refinement are shown on the right. (**B**) Slices through the density of the four bodies after the consensus refinement (top) and after multi-body refinement (down). (**C**) Local resolution estimates (in Å) calculated in RELION after the consensus refinement (left) and after multi-body refinement (right). (**D**) The contributions of all eigenvectors to the variance. The second eigenvector, for which the maps at the extremes are shown in panel E, is highlighted in red. (**E**) Motion represented by the second eigenvector, *cf* ***Video 4***. The helix that connects the core of the spliceosome and the LSm ring of the SF3b body that gets broken during the repositioning of the bodies in the eigenvector movies and the combined maps is indicated with an asterisk (also see main text).

DOI: https://doi.org/10.7554/eLife.36861.010

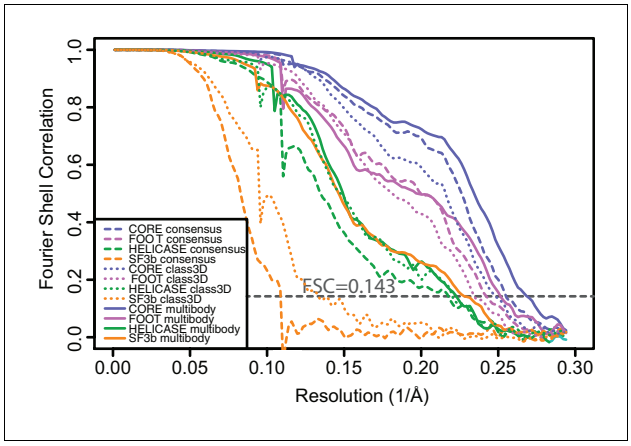

Figure 3—figure supplement 1. Fourier shell correlation curves calculated from independently refined halves of the data for the four bodies after consensus refinement (dashed lines), for the largest class of a discrete 3D classification (dotted lines) and after the second multi-body refinement (solid lines).

DOI: https://doi.org/10.7554/eLife.36861.011

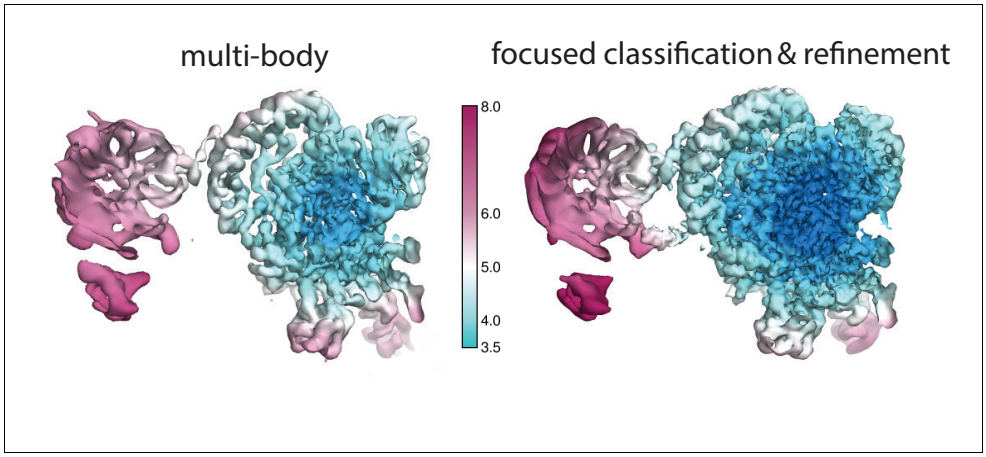

Figure 3—figure supplement 2. Local resolution estimates (in Å) for the SF3b region after multi-body refinement (left) and after subsequent partial signal subtraction in relion_flex_analyse followed by focused classification and refinement of the best class (right).

DOI: https://doi.org/10.7554/eLife.36861.012

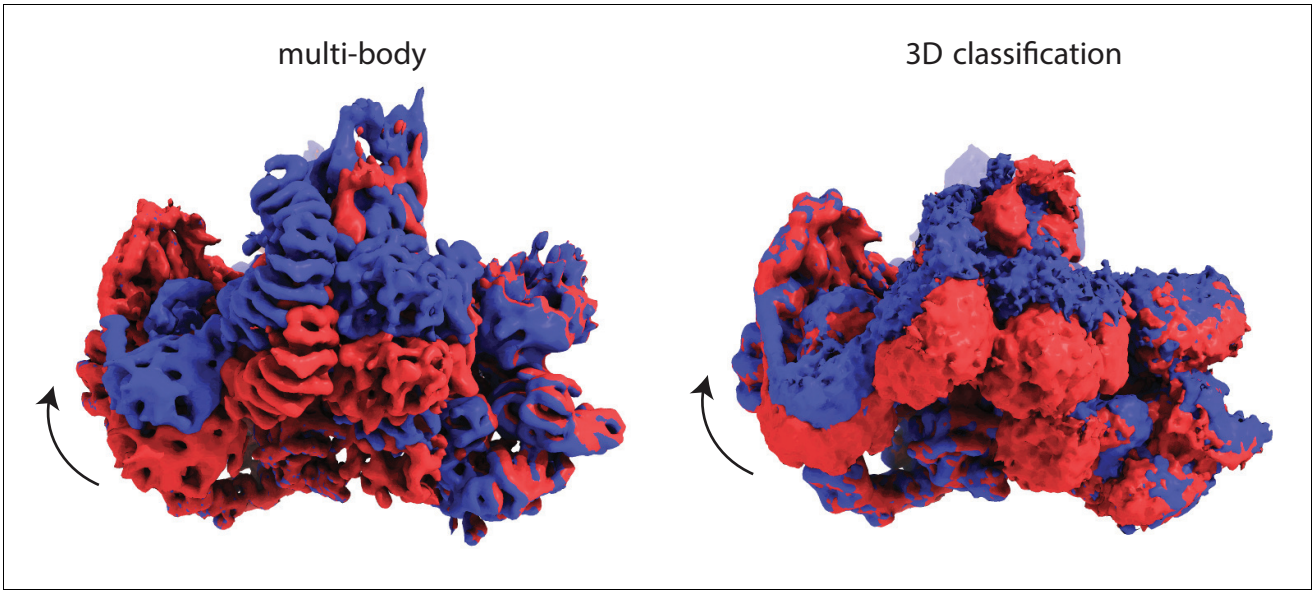

Figure 3—figure supplement 3. The largest two classes of a 3D classification with eight classes (right) represent a similar motion as identified by the first principal component from the multi-body approach (left). For the latter, the third and eight out of ten movie frames are shown.
DOI: https://doi.org/10.7554/eLife.36861.013